Journal of Materials Chemistry C

ROYAL SOCIETY OF CHEMISTRY

PAPER

View Article Online
View Journal | View Issue

Cite this: J. Mater. Chem. C, 2026, 14, 6808

Ferroelectric and hyper dielectric modes in ferronematic liquid crystals

Rahul Uttam, [a] Neelam Yadav, [a] Mudit Sahai,[ae] Alexander Belik,[a] Wanhe Jiang,[c] Georg H. Mehl, *[cd] Jagdish K. Vij *[a] and Yuri P. Panarin *[ab]

Received 2nd January 2026,
Accepted 5th February 2026

DOI: 10.1039/d6tc00004e

rsc.li/materials-c

Binary mixtures of the ferronematic liquid crystal **DIO** with the recently reported non-ferroelectric liquid crystalline material **WJ-16** exhibiting colossal permittivity (CP) ≈ 5000 and superparaelectricity were studied by polarizing optical microscopy (POM), electrical switching, and dielectric spectroscopy. Three mixtures with different **WJ-16** concentrations ranging from 10, 25 to 50% (w/w) in **DIO** as the host were prepared. Our original expectation was the observation of new nematic compositions with both ferroelectric nematic (N_F) and the non-ferroelectric CP phases. We found that the non-ferroelectric phase in mixtures exhibits a CP mode, originally observed in pure **WJ-16**. Dielectric spectroscopy of mixtures shows two distinct relaxation processes: the typical paraelectric response and the CP mode. This CP mode in the mixtures is not superparaelectric, and here it is defined as a hyper-dielectric mode. This is the first direct demonstration of the mixtures having both ferroelectric and hyper-dielectric phases in liquid crystalline materials.

1. Introduction

Ferroelectric nematics were observed independently in two different nematic compounds, **DIO**[1] and RM-734,[2] and the discovery has generated great interest. Ferroelectric nematics are characterized typically by (i) extremely large dipole moments ($\mu \sim >9$ D), (ii) high spontaneous polarization ($P_s \sim 5\ \mu C\ cm^{-2}$)[3–6] and (iii) colossal dielectric permittivity (CP) ∼ 10 000. Such high values of the dielectric permittivity are modeled by two different theoretical models: the high-ε model[7,8] conceptually based on a ferroelectric Goldstone (phason) mode, and the polarization-external capacitance Goldstone reorientation model[9–11] taking into account coupling of the Goldstone mode with the external capacitance of the measuring cell, particularly through insulating surface layers at the electrodes.

Though new ferroelectric LCs[12–20] are reported and discussed continuously, the discovery of ferroelectric nematics has not yet brought clear benefits to the electro-optic (EO) switching and liquid crystal display (LCD) industries. On the other hand, the huge or the colossal dielectric permittivity (CP) observed in ferroelectric nematics is a potential working medium in supercapacitors for future prospective applications. Supercapacitors are characterized by very large capacitances (1 mF to >10 kF) which can combine the properties of capacitors and batteries into one device, hence these can be used in two rather independent applications: (a) as batteries, *i.e.*, storage of electrical energy and (b) as electronic components. Supercapacitor batteries are based on different storage mechanisms, such as the accumulation of ions in a double layer or electrochemical reactions arising from a combination of ions. The specific electrical capacity of a typical supercapacitor is about 10 kW kg^{-1}, an order of magnitude higher than that of the lithium-ion batteries, and supercapacitors also have faster charge/discharge cycles.[21] This property is especially important in applications that require rapid bursts of energy to be released from the storage device. A supercapacitor also has the potential to be used as a part of electronic device, where the need for increased device density goes hand in hand with a miniaturization of electronic structures down to the nanoscale. There, the replacement of conventional dielectric materials with those of colossal dielectric permittivity is required. We note that beyond ferroelectric nematics and solid ferroelectrics, CP is also observed in solid non-ferroelectric materials known as superparaelectrics (SPEs).

There are no strict definitions of the terms ferro-, para-, and superpara-electrics, as they have mostly been introduced as electrical analogs of the terms used for magnetic materials. The first systematic studies were carried out by the Curie brothers in 1880 when they first described the piezoelectric effect.[22]

[a] Department of Electronic and Electrical Engineering, Trinity College Dublin, The University of Dublin, Dublin 2, Ireland. E-mail: yuri.panarin@tudublin.ie, jvij@tcd.ie
[b] Department of Electrical and Electronic Engineering, TU Dublin, Dublin 7, Ireland
[c] Department of Chemistry, University of Hull, Hull HU6 7RX, UK. E-mail: g.h.mehl@hull.ac.uk
[d] Department of Materials Science & Engineering, Xi'an Jiaotong University, Xi'an, China
[e] Department of Physics, Birla Institute of Technology and Science, Pilani, Rajasthan, India

In 1912, Debye pointed out that this class of materials carry a permanent electric dipole moment, making the analogy to ferromagnetics. Following Langevin's theory of paramagnetism, Debye derived the equation $(\varepsilon - 1)/(\varepsilon + 2) = a + b/T$, where a is proportional to the density of the substance and b to the square of the electric dipole moment to describe the dielectric properties. As per this equation, $T_C = b/(1 - a)$, for a critical temperature T_C, the value of the dielectric constant reaches infinity. Debye proposed that T_C is the analog of the Curie temperature of a ferromagnet. Furthermore, in 1912, based on Debye's model, Schrödinger speculated that all solids should become "ferroelectric" at sufficiently low temperatures.[23] The first report of classical ferroelectric hysteresis was observed by Valasek in 1921.[24]

Considering that most materials are not ferroelectric, paraelectricity describes the behavior of dielectrics where an applied electric field induces polarization resulting from the alignment of dipoles parallel to the field, and this polarization disappears when the field is removed. Hence, for such materials, the *P–E* dependence obeys the Langevin function, with an initial almost linear *P–E* dependence over a wide range of applied electric fields, and a gradual saturation is reached at much higher fields. For example, the sample, **WJ-16**, shows linear *P–E* dependence even at extremely large electric fields up to 11 V μm^{-1} (ref. 25) and is thus considered almost linear *P vs. E* within the experimental constraints. Also, **WJ-16** is not ferroelectric; it exhibits CP, and it can be described as superparaelectric. The objective for this study is to explore whether mixtures of the two materials **WJ-16** and **DIO**, showing both paraelectric and ferroelectric nematic phases, would allow us to monitor the transition from paraelectric to superparaelectric and to ferroelectric, using carefully constructed compositions in these two materials, whose chemical structures are very close.

To our surprise, the experimental results in the mixtures show that we found the first examples of materials that show a sequence of two nematic phases: ferroelectric and superparaelectric.

2. Materials

This paper reports a study of the different mixtures of two different types of nematic LCs: (i) a well-known ferroelectric nematic **DIO** and (ii) a recently reported non-ferroelectric, but superparaelectric nematic **WJ-16**.[25] The molecular structure of **WJ-16** is based on **DIO**, where a fluorophenyl group of **DIO** is replaced by a pyrimidine group, as shown in Fig. 1, and this replacement increases the molecular dipole moment from 9.4 D for **DIO** to 10.4 D for **WJ-16**. Furthermore, the phenylpyrimidine unit in **WJ-16** is more planar than the biphenyl unit of **DIO**. Surprisingly, **WJ-16** does not show the ferroelectric nematic phase, nevertheless, it also exhibits CP. This was explained in ref. 26 and 27, which showed that a high value of the dipole moment is important, but this is not a sufficient condition for the formation of the N_F phase.

The transition temperatures of individual components and their mixtures are given in Table 1, and the phase diagram is shown in Fig. 2.

At first glance, the phase sequences of mixtures appear similar to that of **DIO**. However, in **DIO**, "N" is an ordinary nematic phase, but in **WJ-16** and mixtures, "N" is a superparaelectric nematic phase with CP as discussed below; the concentration where CP values increase is yet to be determined.

3. Results and discussion

3.1. Polarizing optical microscopy (POM)

The temperature-dependent optical textures of the prepared mixtures were investigated using polarizing optical microscopy (POM) in different cells with thicknesses ranging from 2 to 9 μm. Both commercially sourced (E.H.C. Co. Ltd, Japan) and laboratory-fabricated "uncoated" indium tin oxide (ITO) electrode cells were used. Planar and homeotropic alignments were achieved by spin-coating appropriate alignment surfactants and subsequently polymerized as layers onto the ITO surfaces of substrates. Fig. 3(a–c) illustrates the POM textures obtained from 9 μm anti-parallel buffed planar cells filled with the mixtures.

On cooling from the isotropic phase, all mixtures form excellent homogeneous planar textures. On further cooling down to the N_F phase, the texture's homogeneity persists with only color variation due to a change in the birefringence. However, in the N_F phase, all three mixtures, including **DIO** (but not **WJ-16**), show a two-domain texture of opposite chirality which can be observed between slightly uncrossed polarizers

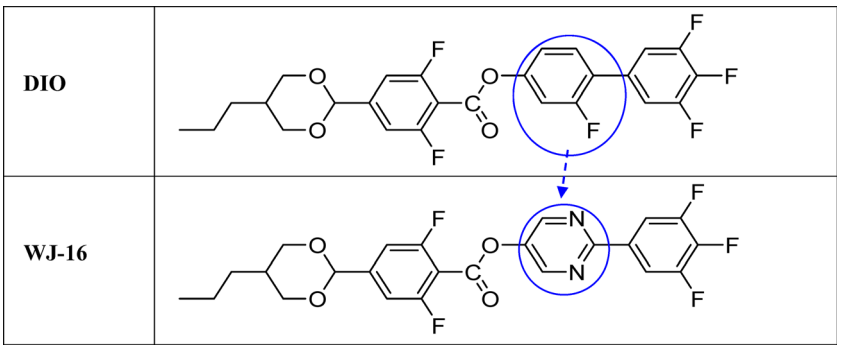

Fig. 1 The chemical structures of molecules **WJ-16** and its prototype **DIO**.

Table 1 The phase sequences and phase transition temperatures (in °C) for different liquid crystal systems and their mixtures

System	Phase sequences determined by Differential Scanning Calorimetry, Dielectric Spectroscopy, electrical switching and texture
DIO	Cr (<20) N_F (66.8) N_x (83.5) N (173.8) Iso
MIX 10 of **WJ-16**	Cr (<20) N_F (52.0) N_x (73.0) N (179.0) Iso
MIX 25 of **WJ-16**	Cr (<20) N_F (50.0) N_x (72.0) N (180.5) Iso
MIX 50 of **WJ-16**	Cr (34.5) N_F (47.5) N_x (66.5) N (190.0) Iso
WJ-16 100%	Cr (79.3) SmA (110.5) N (198.6) Iso

(Fig. 4). Such domains are characteristic of the N_F phase, which appear in anti-parallel rubbed planar cells due to the polar azimuthal anchoring energy.[28] Crystalline phase formation was exclusively observed in MIX 50 at room temperature, the mixture with the highest **WJ-16** concentration (50%). For other mixtures, crystallization was only observed if the sample was kept below room temperature overnight.

In the homeotropically aligned cells, dark optical textures indicative of excellent homeotropic alignment were observed in the N and N_x phases due to the minimal birefringence. In the N_F phase, a more complex, grainy/sandy texture was observed, indicating an emergence of the complex molecular order. In uncoated cells, disordered Schlieren textures were observed in the N and N_x phases. In the N_F phase, a mixture of the Schlieren texture and of a complex domain texture was observed, resulting from an interaction of the polar ordering and of an unaligned cell. The textures observed in both homeotropic and uncoated cells were consistent with those observed for the pure **DIO**.

3.2. Birefringence

Birefringence (Δn) measurements were carried out using an optical spectral technique[29] on a 9 μm homogenous planar-aligned cell. Transmittance (T) spectra were acquired using an Avantes AvaSpec-2048 fiber spectrometer with an achromatic light source, as a function of temperature, spanning from the Iso-N transition to the N_F phase for all mixtures. The transmittance T of a homogeneous planar-aligned cell is given by:

$$T = A\sin^2\left(\frac{\pi\cdot\Delta n(\lambda)\cdot d}{\lambda}\right) + B \quad (1)$$

where A is the amplitude factor, B is the leakage offset of light through the cell, d is the cell thickness, and $\Delta n(\lambda) = k\cdot\frac{\lambda^2\cdot\lambda^{*2}}{\lambda^2-\lambda^{*2}}$ is the birefringence dispersion, governed by the extended Cauchy equation. Birefringence data at a wavelength of 550 nm were calculated using custom-developed software[29] and are presented in Fig. 5.

The temperature dependence of the birefringence in the high-temperature conventional N phase was fitted to the Haller equation, given as:

$$\Delta n(T) = \Delta n_0\cdot Q = \Delta n_0\cdot\left(1-\frac{T}{T_{Iso-N}}\right)^{\beta} \quad (2)$$

where Δn_0 is the maximum birefringence for the order parameter $Q = 1$, T_{Iso-N} is the isotropic to nematic phase transition temperature, and β is the exponent, determined to be 0.2 ± 0.02, for an ordinary/conventional nematic phase. The best fit of the experimental data to eqn (2) confirms the conventional nematic behavior of the high-temperature N phase in the mixtures, with fitting parameters listed in Table 2.

As shown in Fig. 5, the birefringence increases gradually with decreasing temperature in the N phase. Upon transition from the N phase to the N_X or N_F, the birefringence curve deviates from Haller's equation, exhibiting an increased value in the N_x phase on cooling. Subsequently, a discontinuous

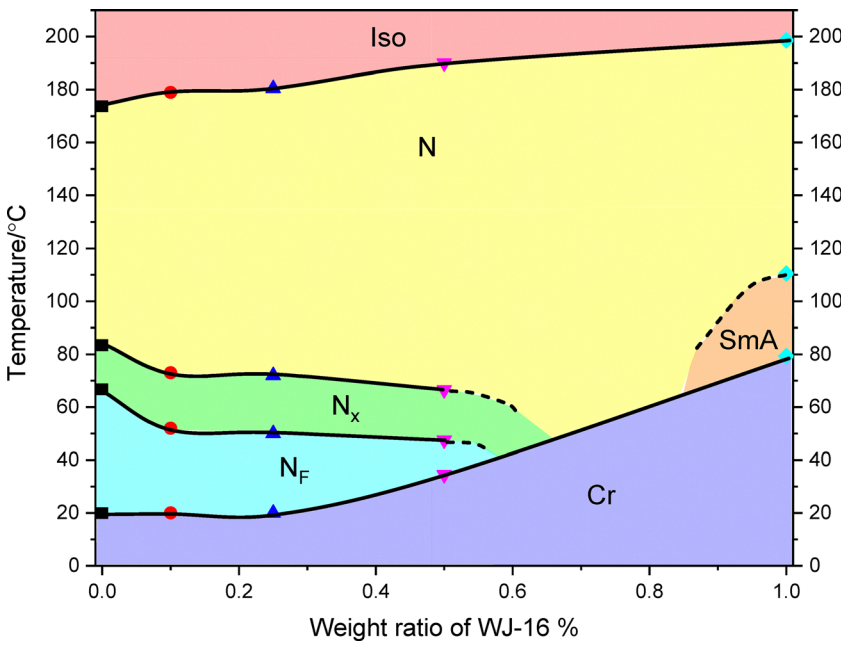

Fig. 2 The phase diagram of **DIO** and **WJ-16** mixtures obtained from DSC, Birefringence, Texture, Dielectric Spectroscopy and electrical switching reversal current.

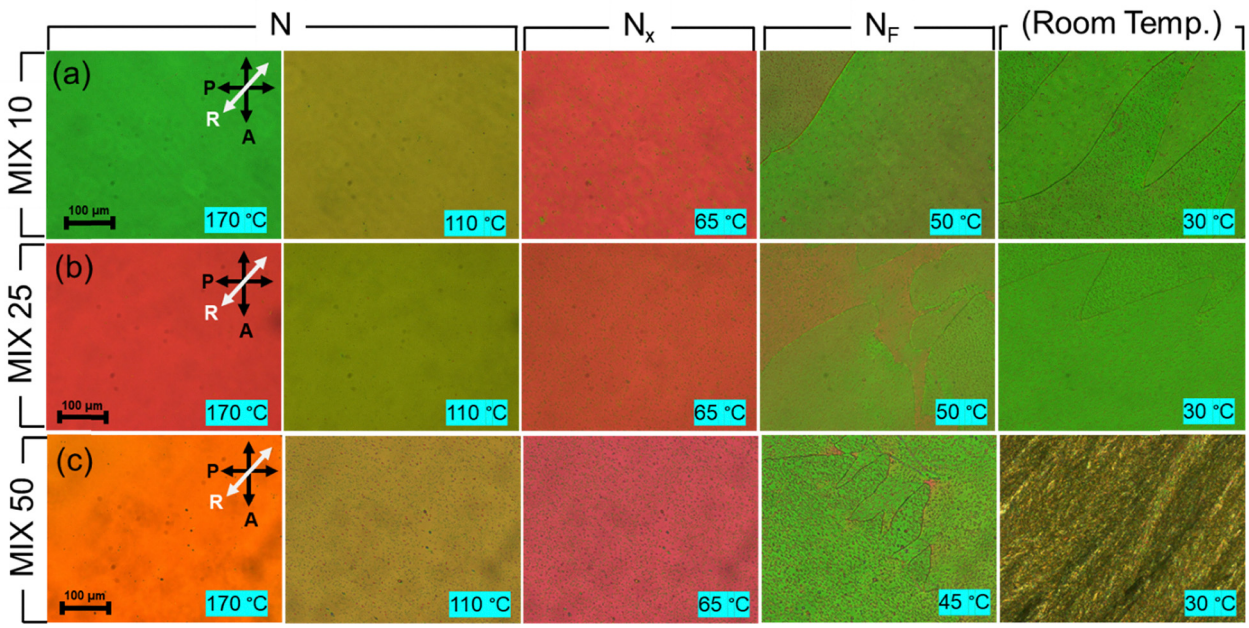

Fig. 3 (a–c). POM textures of 9 µm anti-parallel buffed planar aligned cells, filled with MIX 10, MIX 25, and MIX 50, respectively, were acquired at different temperatures. The analyzer (*A*) and polarizer (*P*) orientations are indicated. The white arrow (*R*) denotes the rubbing direction. The scale bar on the left in Figures represents a length of 100 µm.

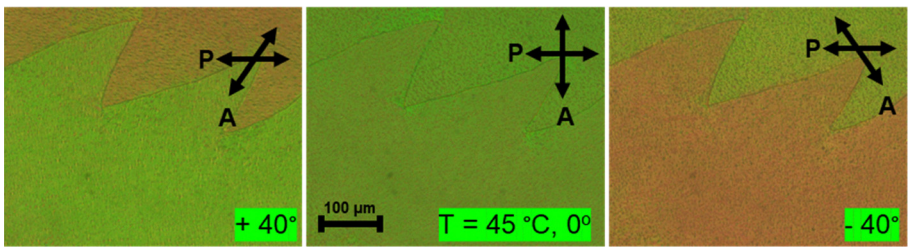

Fig. 4 POM textures of a 9 µm anti-parallel buffed planar cell, filled with MIX 25 at a temperature of 45 °C. Domains of the opposite chirality are observed on the rotation of the polarizer in opposite directions from the crossed polarizer position.

jump in the birefringence is observed at the N_x–N_F transition temperature. The birefringence curves of MIX 10 and MIX 25 are similar to **DIO**. For MIX 50, a dip in the birefringence curve is observed at a temperature of around 60 °C. However, no change in the optical textures is observed (see Fig. 3, MIX 50, T = 45 °C). The observed dip in the birefringence of MIX 50 is assigned to the emergence of both polar and non-polar domains in the intermediate N_x region, as was also observed elsewhere.[31]

3.3. Electrical measurements

A ferroelectric nematic (N_F) phase is characterized by the presence of macroscopic spontaneous polarization (P_s). Here, we examine the ferroelectric behavior of mixtures by using a conventional technique of the reversal switching current.[32] An external electric field of suitable waveform (triangular), generated from an Agilent 33120A signal generator and amplified using a high-voltage amplifier (TReK PZD700), was applied across the liquid crystal cell. The resulting current response across a 1 kΩ resistive load was monitored using a digital oscilloscope.

Fig. 6 shows the switching-current response of a 4 µm planar cell under an applied triangular wave (V_{pp} = 24 V, f = 20 Hz) for (a) **WJ-16**, (b) **DIO**, and (c) MIX 25 in the ferroelectric (N_F) and non-ferroelectric (N) phases, respectively. The appearance of the current reversal peak depends on the temperature, phase, and the frequency of the applied voltage. No peak was observed at higher frequencies (>50 Hz). However, the peaks were observed at lower frequencies, say, 20 Hz in the present case and below, and only in the ferroelectric N_F phase of **DIO** and MIX 25. **WJ-16** shows no spontaneous polarization switching peak in the full temperature range, including the N and SmA phases, confirming that this material does not have a ferroelectric phase. For **DIO** in the N_F phase, a sharp, well-defined peak in the current transient confirms the existence of spontaneous polarization, whereas in the N phase, the absence of a current peak confirms the paraelectric behavior.

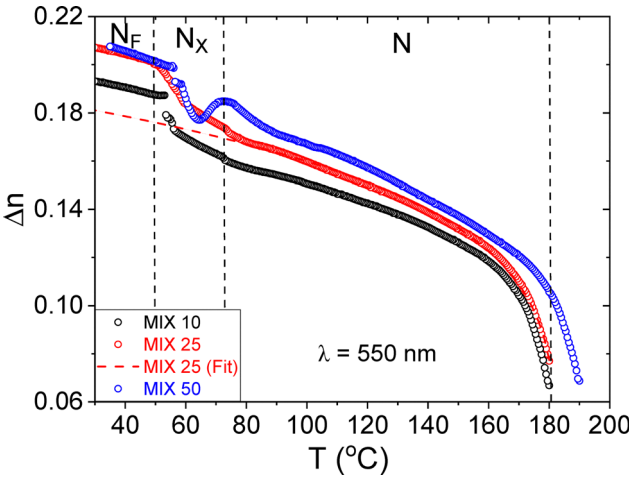

Fig. 5 The temperature dependence of birefringence (Δn) for MIX 10, MIX 25, and MIX 50 measured for a wavelength of λ = 550 nm using a 9 μm homogeneous planar-aligned cell. The experimental birefringence data fitted to Haller's equation (dashed red line) for MIX 25 are shown as an example of fit accuracy. The vertical dotted lines show the phase transitions for MIX 25.

Table 2 Fit parameters of Haller's equation for the experimental birefringence data of the **DIO** + **WJ-16** mixtures

System	Δn_0	β	T_{Iso-N}
DIO[a]	0.18	0.18	172.0
MIX 10	0.18	0.19	179.0
MIX 25	0.19	0.20	180.5
MIX 50	0.19	0.22	190.0
WJ16[b]	0.21	0.25	198.6

[a] Values are taken from ref. 30. [b] From ref. 25.

All three binary mixtures show a transient response similar to **DIO**. The response of the MIX 25 (Fig. 6(c)) is shown as an example. The integral of the current peak gives the value of Ps for MIX 25 to be 2.4 μC cm^{-2}, compared to 4.4 μC cm^{-2} in **DIO**.[1]

3.4. Dielectric spectroscopy

3.4.1. Motivation and methodology. Dielectric spectroscopy is one of the most sensitive techniques for studying the ferroelectric and other polar materials/phases. This was successfully employed for the characterization of ferro-[33–36]/antiferro-[37,38] and ferri-electric[39,40] liquid crystalline phases. One of the most important material parameters of LCs is the dielectric anisotropy, $\Delta\varepsilon_a = \Delta\varepsilon_\parallel - \Delta\varepsilon_\perp$, which governs the electro-optic switching and the Freedericksz transition. To obtain the value of dielectric anisotropy, it is necessary to measure the real values of the perpendicular component of dielectric permittivity, $\Delta\varepsilon_\perp$, in planar cells and parallel components of dielectric permittivity, $\Delta\varepsilon_\parallel$, in homeotropic cells. Dielectric spectroscopy measurements over a frequency range of 0.01 Hz–10 MHz were made using a broadband alpha high resolution dielectric analyzer (Novocontrol GmbH, Germany). The commercial cells of 4 μm and 9 μm thicknesses with both homeotropic and planar alignment were used. These commercial cells use ITO electrodes with low sheet resistance (10 Ω □$^{-1}$), which moves the frequency of parasitic ITO peaks (arising from the sheet resistance of ITO in series with the capacitance of the cell) outside the measured frequency range. The measurements were carried out under the application of a weak voltage of 0.1 V, applied across the cell. The temperature of the sample is stabilized to within ± 0.05 °C.

3.4.2. Dielectric spectroscopy of homeotropic cells. Initially, the parallel component of dielectric permittivity $\left(\varepsilon'_\parallel\right)$ was measured. The phase sequences of all three mixtures are similar to **DIO** (Table 1); therefore, the dielectric spectroscopy results for MIX 25 are presented as a typical example. Fig. 7 shows the temperature dependencies of the total dielectric permittivity (*i.e.*, real (ε') and imaginary (ε'') parts of complex permittivity) for the 9 μm homeotropic cell of MIX 25.

Fig. 8(a) shows 2-D dielectric loss spectra at different temperatures for the 3-D plot of dielectric loss shown in Fig. 7(b). The dielectric spectra were analyzed using the Novocontrol WINDETA program. The complex permittivity data were fitted to the Havriliak–Negami equation, as given below, where the dc conductivity [first term in eqn (3)] is also included:[41]

$$\varepsilon^* = -\frac{i\sigma}{\varepsilon_0\omega} + \varepsilon_\infty + \sum_{j=0}^{n}\frac{\Delta\varepsilon_j}{\left[1+\left(i\omega\tau_j\right)^{\alpha_j}\right]^{\beta_j}} \quad (3)$$

here, ε^* is the complex permittivity, and ε_∞ is the high-frequency permittivity. The latter includes electronic and atomic polarizabilities of the material. ω is the angular frequency of the probe field, ε_0 is the permittivity of free space, σ is the dc conductivity, τ_j is the relaxation time, $\Delta\varepsilon_j$ is the dielectric strength of the jth relaxation process, and α_j and β_j are the corresponding symmetric and asymmetric broadening parameters of the distribution of relaxation times.

Fig. 8(b–d) are examples of the fitting of the dielectric loss spectra to three relaxation processes at three different temperatures: 80 °C, 52 °C, and 35 °C.

There are three relaxation processes observed in the dielectric spectra of mixtures termed as P1–P3, with an increase in the relaxation frequency. The dielectric spectra were fitted to eqn (3) with fixed stretching parameters (α, β), and from the fitting, we obtain β = 1 for all processes. The symmetric stretching parameter α = 1 for both processes P2 and P3, implying that these relaxation processes are of pure Debye type. The symmetric stretching parameter for process P1, α_1, lies in the range of 0.65–0.90 depending on the temperature, implying that this is an ionic mobility process rather than a molecular relaxation process.

Fig. 9 shows the temperature dependencies of the dielectric strengths and relaxation frequencies of the three relaxation processes, P1–P3, and their sum for a 9 μm homeotropic cell deduced from the fitting of the dielectric spectra shown in Fig. 7 and 8.

On examining Fig. 9(a), the temperature dependencies of three relaxation strengths, P1–P3, are observed. The physical nature/origin of the relaxation processes P1–P3 was defined in ref. 25, 42 and 43. The lowest frequency relaxation process, P1, is assigned to the space charge/interfacial polarization arising

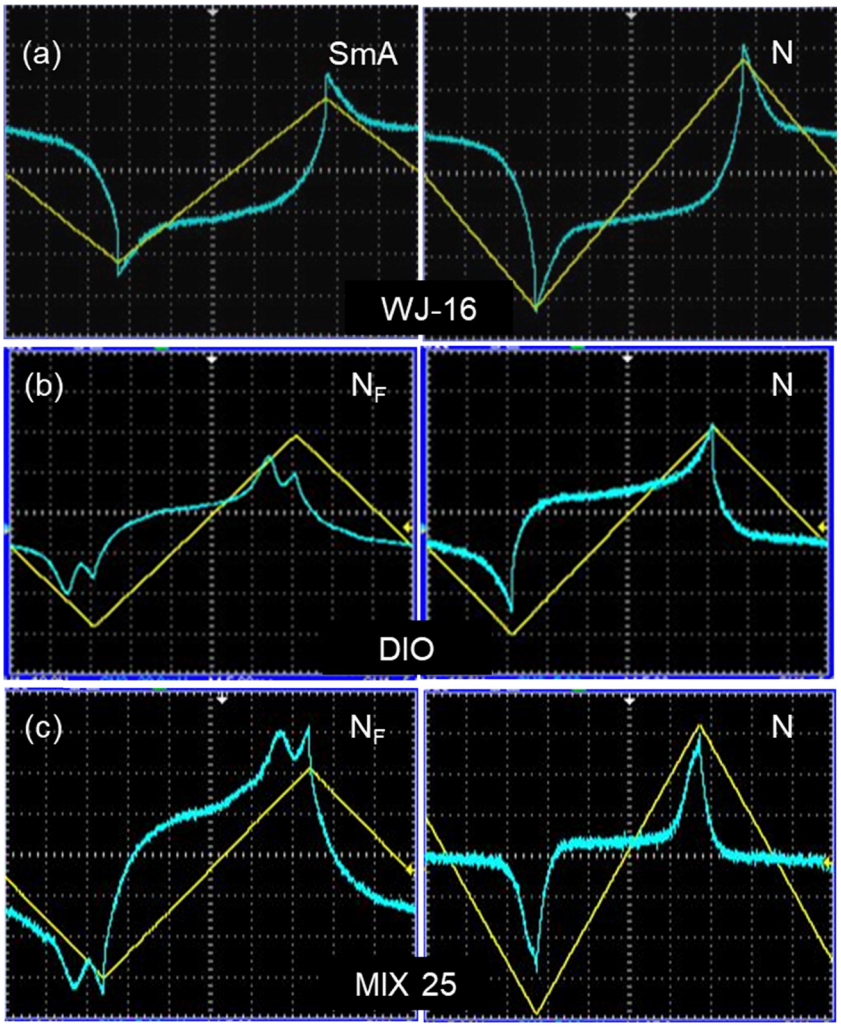

Fig. 6 Switching-current response of a 4 μm homogeneous planar-aligned indium tin oxide (ITO) cell under an applied triangular wave (V_{pp} = 24 V, f = 20 Hz) for (a) **WJ-16**, (b) **DIO**, and (c) MIX 25 in the ferroelectric (N_F) and non-ferroelectric (SmA, N) phases, respectively. The oscilloscope traces show the input applied voltage (Vi, in mV; yellow color), and the output voltage measured across a 1 kΩ resistive load (Vo, in mV; blue color) as a function of time (in s), on the x-axis. The corresponding output current (in mA) is calculated from the measured load voltage using Ohm's law.

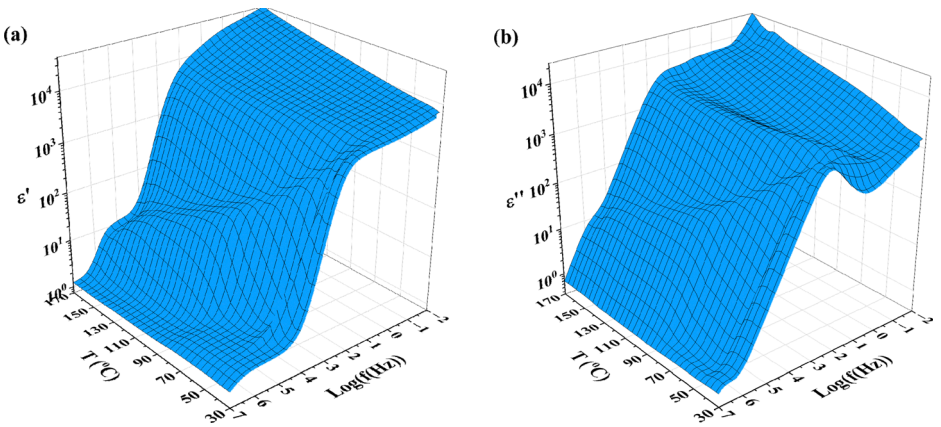

Fig. 7 Temperature dependence of the dielectric spectra of (a) permittivity ε' and (b) loss ε'' measured in a 9 μm MIX 25 homeotropic cell.

from the mobility of ions and, finally, charges accumulating on the electrodes. The dielectric strength of the ionic relaxation process P1 ($\Delta\varepsilon_1$) increases exponentially on heating, which appears as a straight line on the log$y$-axis (see the inset).

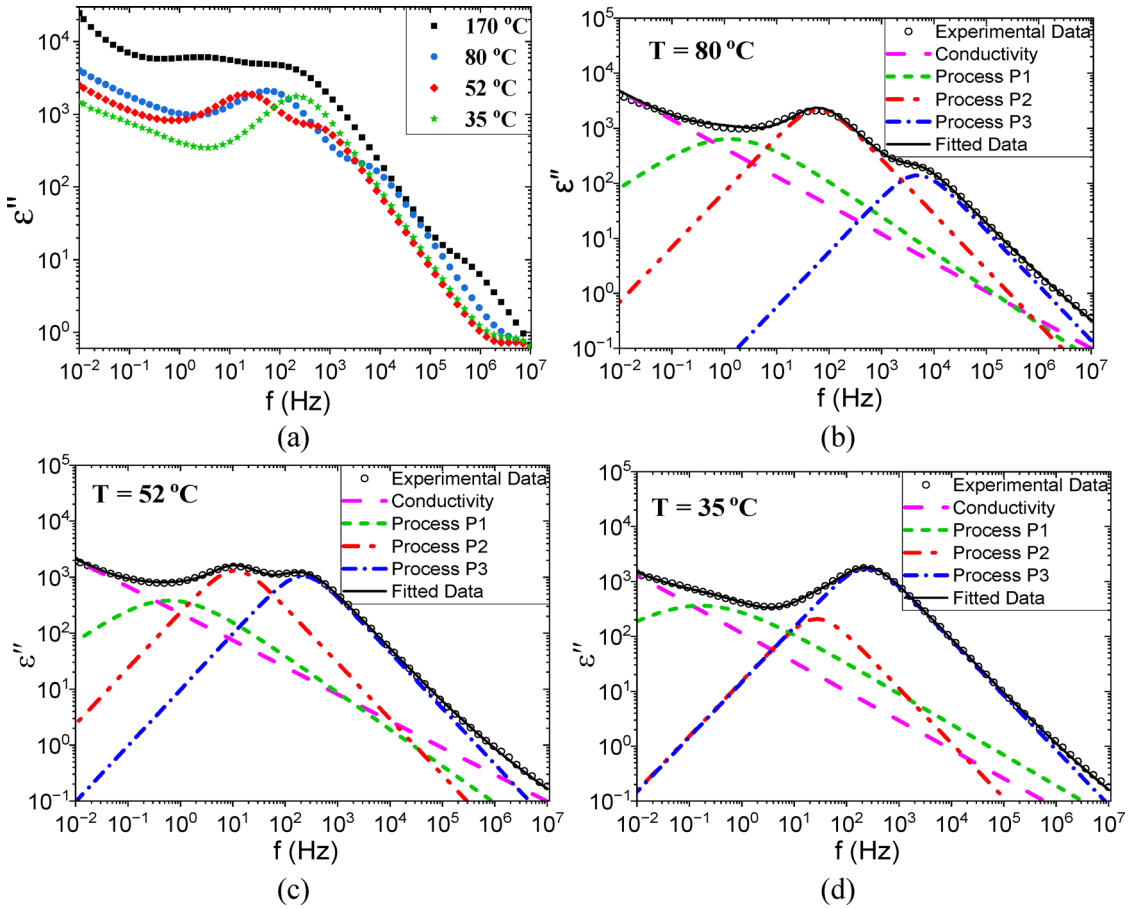

Fig. 8 (a) The frequency dependence of the imaginary part of permittivity (ε'') at different temperatures; analysis shown in (b–d) exhibits examples of fitting of the imaginary part of permittivity to eqn (3) for different temperatures.

The temperature dependence of the dielectric strength of the fastest relaxation process P3 ($\Delta\varepsilon_3$) is typical behavior for the paraelectric-ferroelectric phase transition, similar to P2 in **DIO**. The process P3 corresponds to the rotations around the short molecular axis or the flip–flop mode, as reported in the literature.[42–44] In the isotropic phase, it is purely an individual relaxation process. On cooling to the nematic phase, it gradually transforms into a collective mode with increasing correlation and finally, in the N_X phase, shows Curie–Wiess transition to the ferroelectric phase, similar to P2 in **DIO**. The Nx phase, originally observed in **DIO**, was found to be a density-modulated antiferroelectric, SmZ_A phase,[45] or just a "splay nematic", N_S.[46] Since then, this Nx phase has been reported in a range of additional compounds as well.[44,47,48] Dielectrically, the N_X–N_F phase transition is of the second order, while N–N_F is a first-order phase transition.[49]

The mid-frequency process P2 is very intriguing in nature. This process exists in the entire temperature range and in all phases. It also exhibits colossal permittivity CP (~4500) independent of temperature. This is identical to the second relaxation process (P2) observed in the compound **WJ-16**,[25] though not observed in **DIO**. The physical nature of this process is still unclear and is discussed later in this manuscript.

3.4.3. Dielectric spectroscopy of planar cells. The perpendicular component of the dielectric permittivity ($\varepsilon'_\perp$) was measured in 9 μm commercial planar cells, as shown in Fig. 10. The obtained dielectric spectra were fitted to eqn (3), similar to the homeotropic cells.

Fig. 11 shows the temperature dependencies of the sum of the various dielectric strengths and the relaxation frequencies of the two processes observed in a 9 μm commercial planar cell. A comparison of Fig. 9(a) and 11(a) shows that the temperature dependencies of the dielectric processes are very different. Firstly, in contrast to the homeotropic cell, the ionic process is not observed in the planar cell, and the other two processes correspond to the processes P2–P3. Secondly, and most importantly, the total dielectric strength of the planar cell is independent of temperature or is limited by the combined capacitance of the two alignment layers, similar to the arguments put forward by the Boulder group.[9]

Recently, Clark *et al.* reported an effect of the insulating alignment layers on the apparent/measured values of the dielectric permittivity. It is noted that the apparent capacitance C_{app} of an LC cell is a combination of three capacitances in series: the capacitance of the LC layer C_{LC}, and the two capacitances of the insulating alignment layers, C_{al}. Hence, the

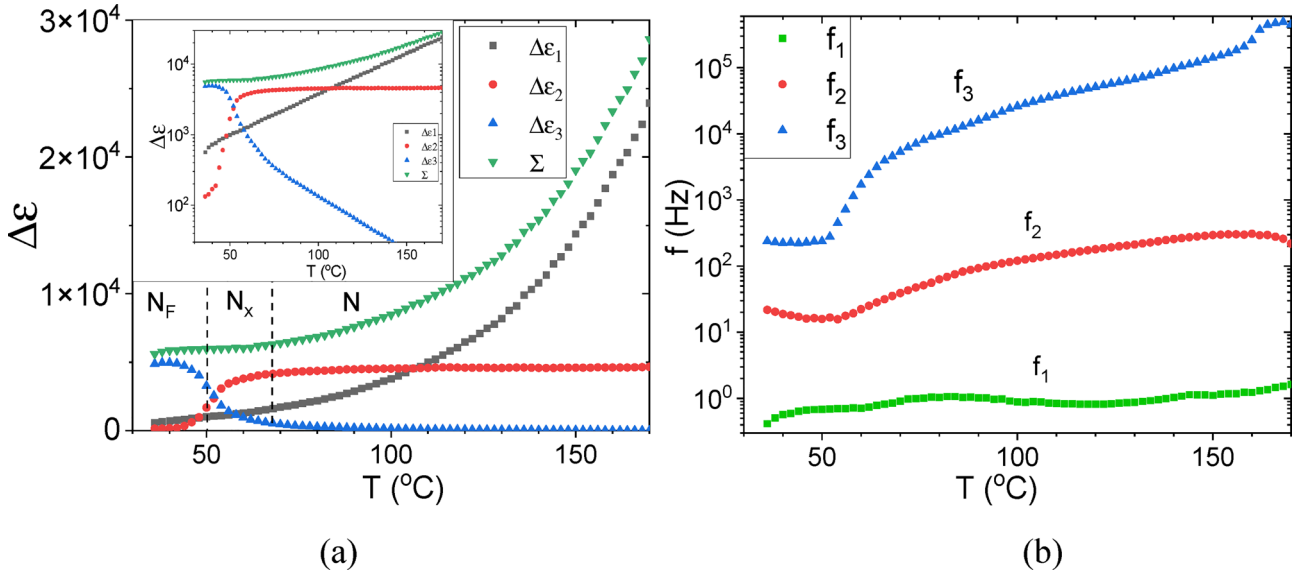

Fig. 9 Temperature dependence of (a) the dielectric strength of different processes and their sum, and (b) relaxation frequencies of MIX 25 in a 9 μm homeotropic cell. The inset in (a) shows the same results but on the scale of the log y-axis.

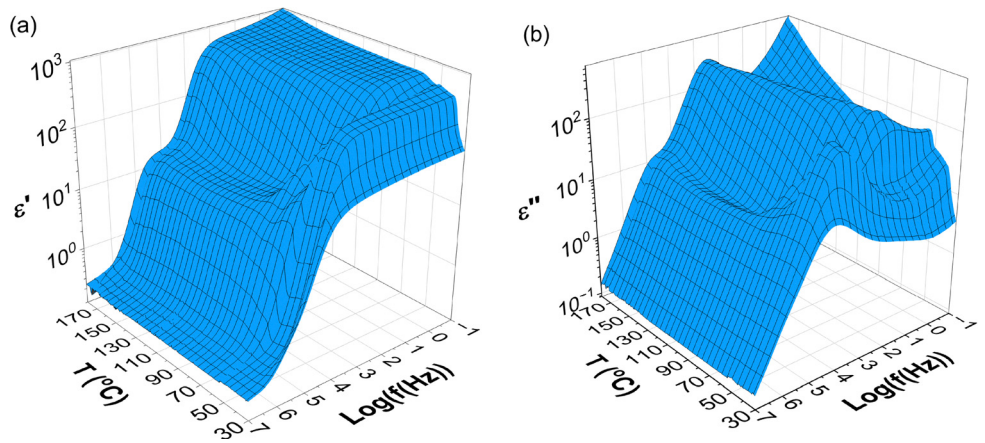

Fig. 10 Temperature dependence of the dielectric spectra of (a) permittivity ε' and (b) loss ε'' measured in a 9 μm MIX 25 antiparallel rubbed planar aligned cell.

total (apparent) capacitance is $C_{app} = \frac{C_{LC} \cdot C_{al}}{C_{LC} + C_{al}}$. In the ordinary case, *i.e.*, having materials with low/moderate dielectric permittivity, the capacitance of the LC cell is $C_{LC} \ll C_{al}$, hence the apparent capacitance is the capacitance of the LC cell, $C_{app} = C_{LC}$. This gives the real value of capacitance and permittivity. However, in materials with very high dielectric permittivity ($\varepsilon > 10\,000$), such as of the ferroelectric N_F phase, the capacitance of the LC cell exceeds the capacitance of the alignment layer, $C_{LC} \gg C_{al}$. In such a case, the apparent capacitance is limited by the capacitance of the insulating layers, C_{al}. We term it as the "alignment layers limit", $C_{app} \lesssim C_{al}$. This means that the apparent dielectric permittivity shows a weak temperature dependence as can be observed in a planar cell; see Fig. 11(a). Therefore, values of the capacitance/permittivity as observed are lower than the real values, and hence these are limited by the capacitance of the alignment layers. However, the dielectric spectroscopy shows two individual dielectric relaxation processes and a phase transition similar to that observed in a homeotropic cell. Another important feature of this limit is the absence of the ionic relaxation process (process P1), because most of the applied voltage is distributed along the alignment layers, and this screens the voltage on the LC layer. Such a limit is also observed in other high ε materials such as the bent-core LCs[50,51] and SPE nematics.[25]

3.4.4. Discussion of the colossal permittivity mode. We now direct our focus towards the mid-frequency relaxation process P2, which exhibits a colossal value of permittivity (~4500), independent of temperature, hereafter referred to as the 'colossal permittivity (CP) mode'. As mentioned before, this process exhibits intriguing behavior, as it persists across the entire temperature range and throughout all observed phases, including the isotropic phase.

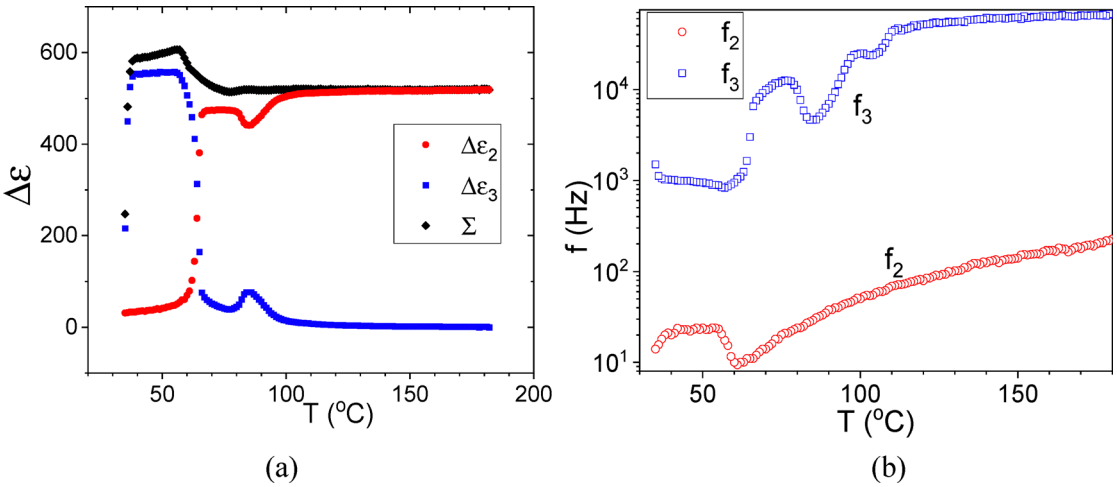

Fig. 11 Temperature dependence of (a) dielectric strengths, and (b) relaxation frequencies of processes P2 and P3 for MIX 25 in a 9 μm antiparallel rubbed planar aligned cell.

This implies that process P2 is not a property of a particular phase, but is a property of the total system. Such a CP mode in the isotropic phase was also observed before and published in several publications.[47,51] The CP mode observed in ref. 51 is temperature-independent and looks identical to the CP mode observed in pure **WJ-16**[25] and in our **WJ-16/DIO** mixtures. Unfortunately, the authors previously did not pay any specific attention to this mode. In this section, we provide a comprehensive discussion and physical interpretation of this mode.

The CP-mode exists in a non-ferroelectric compound, **WJ-16**, which exhibits colossal dielectric permittivity and was therefore initially classified as superparaelectric or SPE.[25] However, based on the results obtained for the mixtures, the data points to a more complex behavior, and hence, requires an update to the above classification. Historically, the term paraelectric refers to a non-ferroelectric phase that, upon cooling, exhibits a transition to the ferroelectric phase described by the Curie–Weiss law. Therefore, the materials without a ferroelectric phase, including **WJ-16**, are simply ordinary dielectrics. As shown in Fig. 9(a), in an ordinary nematic phase, we observed two different relaxation modes: P2 and P3. Process P3 is a paraelectric mode that follows the Curie–Weiss law and relates to the classical paraelectric–ferroelectric transition. The P2 mode exists rather independently along with the paraelectric P3. Considering that this temperature-independent mode exists both in SmA and in the isotropic phase as well, it cannot be related to paraelectric and/or superparaelectric modes. Therefore, strictly speaking, the P2 process here is not in line with the SPE as it exists in a non-paraelectric pure **WJ-16**.[25] Taking into account the CP of P2, it can be called superdielectric. However, this term is already reserved as a working medium in supercapacitors, which might consist of other mechanisms, different from P2, including the ionic process. On considering that the behavior observed here is not connected to a classical para- to ferroelectric transition process, but the materials nevertheless exhibit colossal permittivity (CP). In our view, the behavior is best described as a high-permittivity dielectric mode or, briefly and literally, "HiPer dielectrics" or simply "hyper dielectrics".

Let us now discuss the physical origin of P2. The colossal or high dielectric permittivity reflects an extremely strong collective correlation of molecular dipoles. In the solid SPE materials, this arises from the well-aligned molecular clusters.[52] The dielectric permittivity depends on the size of the ferroelectric-like domains or clusters. These are not only temperature-dependent but also dependent on the size of the sample. In other words, large values of the dielectric permittivity imply a dipolar orientation of the polar clusters over large domains. Such a behavior is reported for some bent-core LCs,[50,51] which contain polar and ferroelectric cybotactic clusters that, in turn, grow upon cooling. In pure **WJ-16** and in its mixtures, such clusters are not observed, and also the dielectric strength is independent of temperature but linearly proportional to the cell thickness.[25] The linear dependence of dielectric permittivity on the cell thickness is a property of the long-range correlated LC systems, and it is well observed in the N_F phase,[8–10] surface-stabilized ferroelectric SmC* phase[36] and in bent-core LCs.[53] This implies that liquid crystals have a long-range directional order, and the correlation length may, to some extent, only be limited by the cell thickness. In such systems, the molecular dynamics and the associated phason mode can be modeled with boundary conditions at the electrodes, which gives a linear dependence of dielectric strength on the cell thickness.[8–10,36]

The dielectric permittivity of P2 is linearly dependent on the cell thickness, and this implies certain similarity with those long-range systems. The higher values of dielectric permittivity can be explained using the classical approach suggested by Kirkwood and Frohlich,[54,55] where the static dielectric permittivity, ε_s, in isotropic liquids is given as:

$$\varepsilon_s \sim \mu^2(1 + z\overline{\cos\gamma}) \quad (4)$$

here, $(\overline{\cos\gamma})$ is the average of the cosine angle between the neighboring molecules, and z is the average number of the

interacting dipoles, also called the coordination number. Assuming $(\overline{\cos\gamma})$ equals unity, the dielectric permittivity is proportional to the square of the dipole moment and to the correlation number, z plus one. Therefore, the CP of P2 in **WJ-16** can be well-explained by the long-range correlation of molecular dipoles, *i.e.* very high or infinite z, even in the isotropic phase. Such a high value of the correlation factor, in turn, may be explained by an extremely large value of the dipole moment. The precise physical-origin of the process observed here is not yet clear and requires further investigations, but it is, in our view, directly associated with the long-range nature of dipole–dipole interactions of the molecules.

4. Conclusions

We investigated binary mixtures of the ferronematic LC **DIO** with the recently reported non-ferroelectric compound **WJ-16**, which shows colossal permittivity. We show data for three mixtures with different concentrations of **WJ-16**, ranging from 10%, 25%, and 50% (w/w) in the host **DIO**. The prepared mixtures were studied by optical methods, broadband dielectric spectroscopy, and electrical switching. The results confirm the presence of a low-temperature ferroelectric phase in all the three mixtures, with a phase sequence similar to **DIO**. Interestingly, the non-ferroelectric phases in mixtures exhibit a CP mode, which is different from the pure **DIO**. This CP mode was originally observed in **WJ-16** and was initially termed superparaelectric. However, the dielectric spectroscopy of the mixtures exhibits two distinct relaxation processes: a typical paraelectric response and an additional CP mode. Therefore, in these mixtures, this CP mode cannot be identified as simply an SPE mode and needs to be redefined as a hyper-dielectric mode. This is the first direct demonstration of materials with both ferroelectric and hyper-dielectric modes present in liquid crystalline materials. Moreover, the high-dipole moment of the constituent molecules of these LCs enable the exploration of new condensed matter physics where the combination of fluidity, self-assembly, and polarity of materials gives rise to novel physical phenomena not observed previously in the solid-state materials having colossal dielectric permittivity. In our view, such materials exhibiting a hyper-dielectric mode have a significantly large potential as a working medium for the prospective supercapacitor industry.

Conflicts of interest

There are no conflicts to declare.

Data availability

The original data can be obtained from one of the corresponding authors of the paper upon reasonable request.

Acknowledgements

The work in Dublin was funded by the US-Ireland, SFI 21/US/3788 and we thank our collaborators in Belfast and Kent State University, USA for ongoing discussions on the topic. WJ thanks the CSC, China, for the award of a PhD scholarship; GHM thanks RCUK and Diamond Light Source for beamline access SM36624 and SM38372.

References

1 H. Nishikawa, K. Shiroshita, H. Higuchi, Y. Okumura, Y. Haseba, S. Yamamoto, K. Sago and H. Kikuchi, *Adv. Mater.*, 2017, **29**, 1702354, DOI: 10.1002/adma.201702354.
2 R. J. Mandle, S. J. Cowling and J. W. Goodby, *Phys. Chem. Chem. Phys.*, 2017, **19**, 11429–11435, DOI: 10.1039/C7CP00456G.
3 X. Chen, E. Korblova, D. Dong, X. Wei, R. Shao, L. Radzihovsky, M. A. Glaser, J. E. Maclennan, D. Bedrov, D. M. Walba and N. A. Clark, *Proc. Natl. Acad. Sci. U. S. A.*, 2020, **117**, 14021–14031, DOI: 10.1073/pnas.2002290117.
4 R. J. Mandle, S. J. Cowling and J. W. Goodby, *Liq. Cryst.*, 2021, **48**, 1780–1790, DOI: 10.1080/02678292.2021.1934740.
5 N. Sebastian, M. Copic and A. Mertelj, *Phys. Rev. E*, 2022, **106**, 021011, DOI: 10.1103/PhysRevE.106.021001.
6 M. T. Máthé, B. Farkas, L. Péter, Á. Buka, A. Jákli and P. Salamon, *Sci. Rep.*, 2023, **13**, 6981, DOI: 10.1038/s41598-023-34067-1.
7 N. Vaupotič, D. Pociecha, P. Rybak, J. Matraszek, M. Čepič, J. M. Wolska and E. Gorecka, *Liq. Cryst.*, 2023, **50**, 584–595, DOI: 10.1080/02678292.2023.2180099.
8 V. Matko, E. Gorecka, D. Pociecha, J. Matraszek and N. Vaupotič, *Phys. Rev. Res.*, 2024, **6**, L042017, DOI: 10.1103/PhysRevResearch.6.L042017.
9 N. A. Clark, X. Chen, J. E. Maclennan and M. A. Glaser, *Phys. Rev. Res.*, 2024, **6**, 013195, DOI: 10.1103/PhysRevResearch.6.013195.
10 A. Erkoreka, J. Martinez-Perdiguero, R. J. Mandle, A. Mertelj and N. Sebastián, *J. Mol. Liq.*, 2023, **387**, 122566, DOI: 10.1016/j.molliq.2023.122566.
11 A. Adaka, M. Rajabi, N. Haputhantrige, S. Sprunt, O. D. Lavrentovich and A. Jakli, *Phys. Rev. Lett.*, 2024, **133**, 038101, DOI: 10.1103/PhysRevLett.133.038101.
12 J. Li, H. Nishikawa, J. Kougo, J. Zhou, S. Dai, W. Tang, X. Zhao, Y. Hisai, M. Huang and S. Aya, *Sci. Adv.*, 2021, **7**, eabf5047, DOI: 10.1126/sciadv.abf5047.
13 B. Basnet, M. Rajabi, H. Wang, P. Kumari, K. Thapa, S. Paul, M. O. Lavrentovich and O. D. Lavrentovich, *Nat. Commun.*, 2022, **13**, 3932, DOI: 10.1038/s41467-022-31593-w.
14 E. Cruickshank, *Chem. Plus. Chem.*, 2024, **89**, e202300726, DOI: 10.1002/cplu.202300726.
15 H. Kikuchi, H. Matsukizono, K. Iwamatsu, S. Endo, S. Anan and Y. Okumuraet, *Adv. Sci.*, 2022, **9**, 2202048, DOI: 10.1002/advs.202202048.
16 Y. Song, J. Li, R. Xia, H. Xu, X. Zhang, H. Lei, W. Peng, S. Dai, S. Aya and M. Huang, *Phys. Chem. Chem. Phys.*, 2022, **24**, 11536–11543, DOI: 10.1039/D2CP01110G.

17 H. Matsukizono, K. Iwamatsu, S. Endo, Y. Okumura, S. Anan and H. Kikuchi, *J. Mater. Chem. C*, 2023, **11**, 6183–6190, DOI: 10.1039/D2TC05363B.
18 H. Nishikawa and F. Araoka, *Adv. Mater.*, 2021, **33**, 2101305, DOI: 10.1002/adma.202101305.
19 A. Manabe, M. Bremer and M. Kraska, *Liq. Cryst.*, 2021, **48**, 1079–1086, DOI: 10.1080/02678292.2021.1921867.
20 A. A. Marchenko, O. L. Kapitanchuk, Y. Y. Lopatina, K. G. Nazarenko, A. I. Senenko, N. Katsonis, V. G. Nazarenko and O. D. Lavrentovich, *Phys. Rev. Lett.*, 2024, **132**, 098101, DOI: 10.1103/PhysRevLett.132.098101.
21 P. Simon and Y. Gogotsi, *Nat. Mater.*, 2008, **7**, 845–854, DOI: 10.1038/nmat2297.
22 J. Curie and P. Curie, Développement par compression de l'électricité polaire dans les cristaux hémièdres à faces inclinées. *Bulletin de la Société Minérologique de France*, 1880, vol. 3(4), pp. 90–93, DOI: 10.3406/bulmi.1880.1564.
23 E. Schrödinger and S. der Kaiserl, *Sitzungsber. Akad. Wiss. Wien, Math.-Naturwiss. Kl., Abt. 2A*, 1912, **121**, 1937–1972.
24 J. Valasek, *Phys. Rev.*, 1921, **17**, 475–481, DOI: 10.1103/PhysRev.17.475.
25 Y. P. Panarin, W. Jiang, N. Yadav, M. Sahai, Y. Tang, X. Zeng, O. E. Panarina, G. H. Mehl and J. K. Vij, *J. Mater. Chem. C*, 2025, **13**, 1507–1518, DOI: 10.1039/D4TC03561E.
26 Y. Song, S. Aya and M. Huang, *Giant*, 2024, **19**, 100318, DOI: 10.1016/j.giant.2024.100318.
27 Q. Liao, S. Aya and M. Huang, *Liq. Cryst. Rev.*, 2024, **12**, 149–194, DOI: 10.1080/21680396.2025.2478561.
28 X. Chen, E. Korblova, M. A. Glaser, J. E. Maclennan, D. M. Walba and N. A. Clark, *Proc. Natl. Acad. Sci. U. S. A.*, 2021, **118**, e2104092118, DOI: 10.1073/pnas.2104092118.
29 O. E. Panarina, Y. P. Panarin, F. Antonelli, J. K. Vij, M. Reihmann and G. Galli, *J. Mater. Chem.*, 2006, **16**, 842–849, DOI: 10.1039/B509119E.
30 N. Yadav, Y. P. Panarin, W. Jiang, G. H. Mehl and J. K. Vij, *Phys. Chem. Chem. Phys.*, 2023, **25**, 9083–9091, DOI: 10.1039/D3CP00357D.
31 A. Barthakur, J. Karcz, P. Kula and S. Dhara, *Phys. Rev. Mater.*, 2023, **7**, 035603, DOI: 10.1103/PhysRevMaterials.7.035603.
32 N. A. Clark, M. A. Handschy and S. T. Lagerwall, *Mol. Cryst. Liq. Cryst.*, 1983, **94**, 213–233, DOI: 10.1080/00268948308084258.
33 C. Filipic, T. Carlson, A. Levstik, B. Zeks, R. Blinc, F. Gouda, S. T. Lagerwall and K. Skarp, *Phys. Rev. A: At., Mol., Opt. Phys.*, 1988, **38**, 5833, DOI: 10.1103/PhysRevA.38.5833.
34 A. M. Biradar, S. S. Bawa and S. Chandra, *Phys. Rev. A: At., Mol., Opt. Phys.*, 1992, **45**, 7282, DOI: 10.1103/PhysRevA.45.7282.
35 F. Gouda, W. Kuczynski, S. T. Lagerwall, M. Matuszczyk, T. Matuszczyk and K. Skarp, *Phys. Rev. A: At., Mol., Opt. Phys.*, 1992, **46**, 951, DOI: 10.1103/PhysRevA.46.951.
36 Y. P. Panarin, Y. P. Kalmykov, S. T. Mac Lughadha, H. Xu and J. K. Vij, *Phys. Rev. E: Stat. Phys., Plasmas, Fluids, Relat. Interdiscip. Top.*, 1994, **50**, 4763, DOI: 10.1103/PhysRevE.50.4763.
37 M. Fukui, H. Orihara, A. Suzuki, Y. Ishibashi, Y. Yamada, N. Yamamoto, K. Mori, K. Nakamura, Y. Suzuki and I. Kawamura, *Jpn. J. Appl. Phys.*, 1990, **29**, L329, DOI: 10.1143/JJAP.42.4453.
38 Y. P. Panarin, O. E. Kalinovskaya and J. K. Vij, *Liq. Cryst.*, 1998, **25**, 241–252, DOI: 10.1080/026782998206399.
39 K. Hiraoka, A. Taguchi, Y. Ouchi, H. Takezoe and A. Fukuda, *Jpn. J. Appl. Phys.*, 1990, **29**, L103, DOI: 10.1143/JJAP.29.L103.
40 Y. P. Panarin, O. E. Kalinovskaya, J. K. Vij and J. W. Goodby, *Phys. Rev. E: Stat. Phys., Plasmas, Fluids, Relat. Interdiscip. Top.*, 1997, **55**, 4345, DOI: 10.1103/PhysRevE.55.4345.
41 S. Havriliak and S. Negami, *Polymer*, 1967, **8**, 161–210, DOI: 10.1016/0032-3861(67)90021-3.
42 N. Yadav, Y. P. Panarin, J. K. Vij, W. Jiang and G. H. Mehl, *J. Mol. Liq.*, 2023, **378**, 121570, DOI: 10.1016/j.molliq.2023.121570.
43 N. Yadav, Y. P. Panarin, J. K. Vij, W. Jiang and G. H. Mehl, *Liq. Cryst.*, 2023, **50**, 1375–1382, DOI: 10.1080/02678292.2023.2219238.
44 S. Brown, E. Cruickshank, J. M. D. Storey, C. T. Imrie, D. Pociecha, M. Majewska, A. Makal and E. Gorecka, *ChemPhysChem*, 2021, **22**, 2506–2510, DOI: 10.1002/cphc.202100644.
45 X. Chen, V. Martinez, E. Korblova, G. Freychet, M. Zhernenkov, M. A. Glaser, C. Wang, C. Zhu, L. Radzihovsky, J. E. Maclennan, D. M. Walba and N. A. Clark, *Proc. Natl. Acad. Sci. U. S. A.*, 2023, **120**, e2217150120, DOI: 10.1073/pnas.2217150120.
46 N. Sebastián, M. Copic and A. Mertelj, *Phys. Rev. E*, 2022, **106**, 021001, DOI: 10.1103/PhysRevE.106.021001.
47 M. Mrukiewicz, M. Czerwinski, N. Podoliak, D. Repcek, P. Perkowski, R. J. Mandle and D. Węgłowska, *J. Mater. Chem. C*, 2024, **12**, 7214–7224, DOI: 10.1039/D4TC01038H.
48 P. Nacke, A. Manabe, M. Klasen-Memmer, X. Chen, V. Martinez, G. Freychet, M. Zhernenkov, J. E. Maclennan, N. A. Clark, M. Bremer and F. Giesselmann, *Sci. Rep.*, 2024, **14**, 4473, DOI: 10.1038/s41598-024-54832-0.
49 M. Mrukiewicz, P. Perkowski, J. Karcz and P. Kula, *Phys. Chem. Chem. Phys.*, 2023, **25**, 13061–13071, DOI: 10.1039/D3CP00714F.
50 L. Guo, E. Gorecka, D. Pociecha, N. Vaupotič, M. Čepič, R. A. Reddy, K. Gornik, F. Araoka, N. A. Clark, D. M. Walba, K. Ishikawa and H. Takezoe, *Phys. Rev. E: Stat., Nonlinear, Soft Matter Phys.*, 2011, **84**, 031706, DOI: 10.1103/PhysRevE.84.031706.
51 S. Nakasugi, S. Kang, T. M. Chang, T. Manaka, H. Ishizaki, M. Sone and J. Watanabe, *J. Phys. Chem. B*, 2023, **127**, 6585–6595, DOI: 10.1021/acs.jpcb.3c02259.
52 Y.-H. Chu, *Science*, 2021, **374**, 33–34, DOI: 10.1126/science.abl9130.
53 L. Guo, E. Gorecka, D. Pociecha, N. Vaupotic, M. Cepic, R. A. Reddy, K. Gornik, F. Araoka, N. A. Clark, D. M. Walba, K. Ishikawa and H. Takezoe, *J. Mol. Liq.*, 2011, **84**, 031706, DOI: 10.1103/PhysRevE.84.031706.
54 H. Fröhlich, *Theory of Dielectrics*, Oxford University Press, 1958.
55 J. G. Kirkwood, *J. Chem. Phys.*, 1939, **7**, 911–919, DOI: 10.1063/1.1750343.

